Journal of Materials Chemistry A

Accepted Manuscript

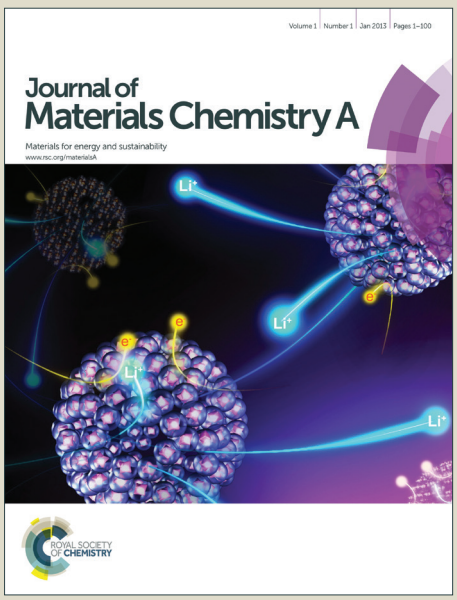

ROYAL SOCIETY OF CHEMISTRY

www.rsc.org/materialsA

Electrocatalytically active cobalt-based metal-organic framework with incorporated macroporous carbon composite for electrochemical applications

Yufan Zhang, Xiangjie Bo*, Anaclet Nsabimana, Ce Han, Mian Li, and Liping Guo*

Faculty of Chemistry, Northeast Normal University, 130024 Changchun, P R China

Abstract

A cobalt-based MOF (Co-MOF) and macroporous carbon (MPC) composite has been prepared for the first time, carried out by a one-step hydrothermal synthesis treatment of the Co-MOF precursor mixture and MPC. The carbon skeleton exhibited a restriction effect on the growth of Co-MOF crystallites, and thus, the sizes of the crystallites matched well with those of the macropores of the MPC matrix. The formation of the composite material was verified by detailed characterization (e.g., X-Ray diffraction, Fourier transform infrared, X-ray photoelectron spectroscopy, energy dispersive X-ray, and thermogravimetric) analyses. It is found that the nanosized and nanocrystalline Co-MOF obtained by the incorporation of MPC greatly improved the electrochemical activity of the composite. More importantly, this composite can be used as a good electrochemical sensing platform, which displays excellent electrocatalytic ability for the oxidation of hydrazine and reduction of nitrobenzene.

Keywords: Electrocatalytical; Metal organic frameworks; Macroporous carbon

* Corresponding author: Tel.: +86 0431 85099762; Fax: +86 0431 85099762.
E-mail address: guolp078@nenu.edu.cn (L.P. Guo) baoxj133@nenu.edu.cn (X.J. Bo).

1. Introduction

Over the past decade, extensive work in the field of materials science has been devoted to the study, characterization and analysis of the metal-organic frameworks (MOF). Their high thermal stability and large surface area as well as their high porosity and crystalline character make them compelling candidates for applications involving gas adsorption and storage[1, 2], chemical separation[3], and drug delivery[4, 5]. With the development of nanoscience and nanotechnology, the precise chemical modification can endow MOF with specific functions and afford a possibility for designing new generation of applications in the field of catalysis[6-10] (chemical, optical, and electrochemical catalysis). Especially, MOF have received more and more attention in electrochemical applications. Mao et al. have described the first demonstration of the use of copper-based MOF as electrocatalysts in oxygen reduction reactions (ORR)[11]. The electrocatalytic reduction of carbon dioxide at copper-based MOF film surface has been reported by Kumar et al[12]. However, single-phase MOF has rarely been utilized for conductivity-based sensing applications, because the majority of MOF are insulators. Thus, heterogeneous nanostructured materials with multi-nanocomponents, especially for conductive nanoparticles such as carbon materials have been proposed[13-15]. For example, a kind of MOF-5 and graphene oxide nanocomposite materials, which combine the favorable attributes of carbonaceous graphene surfaces and MOF, has been prepared by Petit and Bandosz[16]. Lee et al. revealed a composite material,

assembled from azobenzene functionalized graphene oxide and stilbene-MOF[17]. Besides these reports, the much research of Loh's group is also meaningful and interesting. They synthesized a series of MOF-carbon nanocomposite materials. First, they demonstrated that benzoic acid-functionalized graphene can act as a structure-directing template in influencing the crystal growth of MOF[18]. Second, a graphene-porphyrin MOF composite, which shows enhanced catalytic activity for ORR, has been prepared by reacting the pyridine functionalized graphene with iron-porphyrin[19]. And then, a composite made from the assembly of graphene oxide and copper-centered MOF shows good performance as a tri-functional catalyst in three important electrocatalysis reactions, namely: the hydrogen evolution reaction (HER), oxygen evolution reaction (OER), and ORR[20]. Recently, our group has studied the MOF-carbon combination composites[21]. Macroporous carbon (MPC) materials are essential for many modern applications, due to their favorable properties including good thermal and mechanical stability[22, 23]. Especially, the combination of large specific surface area and high electrical conductivity makes MPC very promising as a support platform for MOFs. Herein, a cobalt-based MOF (Co-MOF) material serves as a robust MOF electrococatalyst for this study[24]. Since carboxylic groups and defect sites are present on the MPC surface, it is expected that they might anchor Co-clusters. Thus, we demonstrate the facile preparation of novel Co-MOF nanoparticle-MPC (Co-MOF-MPC) nanocomposites for the first time,

carried out by a one-step hydrothermal synthesis treatment of the Co-MOF precursor mixture and MPC. The composites are referred to as Co-MOF-MPC-*x* (x=*1*, *2*, and *3*), where *1*, *2*, and *3* represent the different contents of MPC in the samples, respectively. Hydrazine and nitrobenzene were selected as marking molecules to evaluate the electrochemical activity of the Co-MOF-MPC composite. The as-prepared Co-MOF-MPC exhibits significant catalytic activity for the oxidation of hydrazine and reduction of nitrobenzene, which indicates that the Co-MOF-MPC composite may hold great promise for the design of electrochemical environmental sensors.

2 Experimental

2.1. Materials.

Hydrazine and nitrobenzene were obtained from Sigma. $CoCl_2 \cdot 6H_2O$, 5-(4-pyridyl)tetrazole (4-H-ptz), 1,3-bi(4-pyridyl)propane (bpp), and NaN_3 were used as purchased from Beijing Chemical Co. Ltd. All other reagents were of analytical grade, and all solutions were prepared with double distilled water.

2.2. Apparatus.

All the electrochemical experiments were performed with a CHI 830B electrochemical Analyzer (CH Instruments, Shanghai Chenhua Instrument Corporation, China) and a PARSTAT 2273 (AMETEK Instruments, USA) electrochemical workstation. A conventional three electrode cell was used, the working electrode used was glassy carbon electrode (GCE) or the modified

electrode, a platinum electrode was applied as the counter electrode and an Ag/AgCl (in saturated KCl solution) electrode served as a reference electrode. All potentials in this paper were measured and reported versus Ag/AgCl. In this study, all the sample solutions were purged with purified nitrogen for 20 min to remove oxygen prior to the beginning of a series of experiments and all experiments were carried out at laboratory temperature. X-Ray diffraction (XRD) patterns were obtained on an X-ray D/max-2200vpc (Rigaku Corporation, Japan) instrument operated at 40 kV and 20 mA using Cu Kα radiation (k = 0.15406 nm). Fourier transform infrared (FT-IR) spectroscopy of the sample was recorded with Nicolet Magna 560 FT-IR spectrometer with a KBr plate. Nitrogen adsorption–desorption isotherms were measured on ASAP 2020 Micromeritics (USA) at 77 K. The Brunauer-Emmett-Teller (BET) method was utilized to calculate the specific surface area. Scanning electron microscopy (SEM) images and energy-dispersive X-ray spectra (EDX) were determined with a Philips XL-30 ESEM operating at 3.0 kV. Thermogravimetric analysis (TGA) was performed on a PerkinElmer Diamond TG Analyzer. X-ray photoelectron spectroscopy (XPS) was measured using Thermo ESCA LAB spectrometer (USA).

2.3. Preparation of MPC.

The SiO_2 template was prepared by the typical Stöber's method[25]. The carbon was introduced into the interstices of the template using the modified method of Jun et al[26]. In a typical synthesis, 2.0 g of sucrose was dissolved in

10 mL aqueous solution containing 0.15 mL of 98% H_2SO_4. 2.0 g of SiO_2 template was immersed into sucrose solution and kept in vacuum for 3 h at room temperature for thorough impregnation. Then the mixture was heated at 100 ºC for 6 h, followed by heating at 160 ºC for a further 6 h for polymerization of sucrose. The solid was subsequently carbonized at 900 ºC in N2 for 3 h in a tube oven. The SiO_2 template was then etched away by overnight dissolution in 10% aqueous HF to leave behind a MPC.

2.4. Synthesis of Co-MOF and Co-MOF-MPC.

The Co-MOF was prepared as reported previously[24]. The $[Co_2(4\text{-ptz})_2(bpp)(N_3)_2]_n$ was studied in our work. In a typical synthesis, 95.2 mg of $CoCl_2 \cdot 6H_2O$, 30 mg of 4-H-ptz, 40 mg of bpp, and 66 mg of NaN_3 were dissolved in 20 mL of de-ionized water with magnetic stirring for 5 min to form well-dissolved mixture suspension. The suspension was filled in a 40 mL of Teflon liner, placed in an autoclave, and heated to 160 ºC for 72 h. The obtained blue powder was recovered by filtration, and then washed with de-ionized water by 3 times. Thereafter, the Co-MOF was obtained by vacuum drying at 60 ºC.

The Co-MOF-MPC composite material was prepared by dispersing MPC powder in the well-dissolved mixture suspension. The resulting suspension was subsequently stirred and subjected to the same synthesis procedure as for Co-MOF. Then, 20 mg, 50 mg, and 80 mg of MPC were added to the f suspension, respectively. The composites are referred to as Co-MOF-MPC-*1*, Co-MOF-MPC-*2*, and

Co-MOF-MPC-*3*, where *1*, *2*, and *3* represent the 20, 50, and 80 mg of MPC in the samples, respectively. The illustration of the preparation of Co-MOFs-MPC-*x* is presented in Scheme 1.

2.5. Preparation of the modified electrodes.

Prior to the modification, GCE (model CHI104, 3 mm diameter) was polished before each experiment with 1, 0.3 and 0.05 μm alumina power, respectively, rinsed thoroughly with double distilled water between each polishing step, and then sonicated successively in 1 : 1 nitric acid, absolute alcohol, and double distilled water. The cleaned electrode was dried with a high-purify nitrogen stream for the next modification. To prepare the modified electrodes, 5 mg of the as-prepared samples were dispersed into 1 mL DMF to give homogeneous suspension upon bath sonication. 5 μL of the suspension was dip-coated onto GCE and the electrode was then dried at room temperature.

3. Results and Discussion

The XRD patterns of Co-MOF-MPC-*1*, *2*, and *3*, as well as pure Co-MOF and MPC are shown in Figure 1A. The diffract peak of MPC at around 21.5° corresponding to 002 crystal plane of carbon is weak and broad (curve a). The profile of Co-MOF showed some sharp peaks between 7.5° and 35° (curve b); and the XRD patterns of Co-MOF-MPC-x as prepared are in good agreement with the standard profile of the Co-MOF. Moreover, compared to the pure Co-MOF, a diffraction hump of Co-MOF-MPC-*x* appears in the range of 20-27°, which originates from the diffract peak of MPC. The obtained materials were further characterized using FT-IR

spectroscopy (Figure 1B). In the region expected for the azido bridges absorption, the pure Co-MOF material exhibits two strong bands at ca. 2098 and 2064 cm^{-1}, attributable to the presence of both μ-EE-N3 and μ-EON3 bridges in the structure[27]. The spectra of Co-MOF-MPC-*x* (curve b-d) largely resemble that of Co-MOF, indicating the presence of Co-MOF in the synthesized composites.

TGA was conducted for the as-prepared precursor in air atmosphere to examine the conversion process during calcinations (Figure 1C). In general, the Co-MOF weight decreases slowly between 30 and 240 °C; this is expected to be due mainly to the removal of chemically adsorbed H_2O. An obvious weight loss is presented between 240 and 330 °C on the TGA curve a; it is believed that thermal decomposition takes place. Similarly, the TGA curve of the Co-MOF-MPC-*2* (curve b) revealed weight loss steps corresponding to the loss of H_2O molecules (30-300 °C), and the decomposition of the organic linkers (300-400 °C), respectively. As can be seen from the Figure 1D, for pure Co-MOF sample, the intense endothermic-exothermal peaks in differential thermal analysis (DTG) curve between 240-330 °C were displayed, which are familiar with the Co-MOF-MPC-*2* in the temperature range of 300-400 °C due to the decomposition of Co-MOF crystallites. The results show the higher thermal stability of Co-MOF-MPC-*2* composites compared with that of pure Co-MOF crystallites; it is due to the encapsulation and protection effect of the carbon matrix. The TGA and DTG curves of Co-MOF-MPC-*1* and *3* were shown in Figure S1.

The textural structures of pure Co-MOF and MPC, as well as Co-MOF-MPC-*2* are shown in Figure 2. The pristine MPC is seen as well-defined interconnected macroporous nanostructure (Figure 2A) with a pore size of about 110 nm. Figure 2B and Figure S2 show that the pure Co-MOF particles are aggregated together with 3D sphere-like nanostructures with diameters around 15-30 μm. In the image of the Co-MOF-MPC-*2* sample (Figure 2C), it is clearly illustrated that the MPC host is homogeneously loaded with the Co-MOF crystals. Indeed, Co-MOF crystallites grow on the surface of MPC matrix, and the spherical morphology of Co-MOF crystallites is around 2 μm, which is smaller than that of the freely growing Co-MOF. It seems that the carbon skeleton exhibited a restriction effect on the growth of Co-MOF crystallites, and thus, the sizes of the crystallites matched well with those of the macropores of the MPC matrix. It is likely that Co-MOF and MPC interact to form new materials having homogenous structure and chemistry. The photograph shows that MPC can retain its monolithic shape before and after impregnation and a crystal growth process, indicating good structure stability. The long range Co-MOF-MPC-*2* morphology is shown in Figure S3. Furthermore, EDX spectra of the as-synthesized composites show the peaks corresponding to carbon, oxygen, and cobalt elements (Figure 2D), confirming the existence of Co-MOF in the Co-MOF-MPC-*2* composites (the Na and Si peaks are caused by the ITO). Further evidence for the grafting of Co-MOF onto the MPC comes from XPS analysis. The elemental components of pure

Co-MOF and Co-MOF-MPC-*x* were summarized in Table S1. Obviously, after the functionalization of Co-MOF using MPC, the relative oxygen content of Co-MOF-MPC-*x* increased due to a lot of oxygen-containing functional groups on the surface of MPC. Figure 3 shows the Co 2p signals of as-made samples. By comparing the pure Co-MOF spectra (Figure 3A) with those of Co-MOF-MPC-*x*, it can be seen that the binding energies for both Co $2p_{3/2}$ and Co $2p_{1/2}$ peaks in Co-MOF-MPC-*x* (Figure 3B-D) are negatively shifted, indicating that the electronic structure of Co atoms were affected to some extent by MPC and implying the electron transfer from MPC to Co. The changes in charge state of the Co core and in adsorption energy of adsorbates on its surface are believed to contribute to the enhancement of its electrochemical activity. The wide survey spectrums of these as-prepared composites are depicted in Figure S4.

Electrochemical impedance spectroscopy (EIS) was applied to analyze the electronic conductivity of different electrode materials (Figure 4). It shows that Co-MOF modified GCE (Co-MOF-GCE) exhibits a semicircle part at high frequency (inset of Figure 4). After being modified with MPC, the semicircle diameter of Co-MOF-MPC-*x*-GCE for EIS markedly decreases. The sequences of the values of charge transfer resistance (R_{ct}) for different electrodes were shown in Table S2 (for five determinations). These results demonstrate that MPC can form good electron pathways between the electrode and electrolyte, and can be expected to be a good platform for sensing applications.

Figure 5A displays the cyclic voltammograms (CVs) of different electrodes for hydrazine. There is almost small electrochemical response at bare GCE or Co-MOF-GCE. An enhanced electrochemical oxidation of hydrazine is exhibited at MPC-GCE. Additionally, the oxidation current of hydrazine at the Co-MOF-MPC-*2*-GCE exhibits a marked increased current signal. The enhanced electrocatalytic activity of Co-MOF-MPC-*2* may be due to the synergistic effect of Co-MOF and MPC. Moreover, the enhanced current could be also the result of the fact that the electrochemically active surface area of Co-MOF-MPC-*2* is much higher than that of Co-MOF. The size of Co-MOF grown on the MPC is smaller than that of the freely growing Co-MOF. The smaller size could supply large active area for the adsorption of reactant molecules and then leads to a high activity. The oxidation of hydrazine at Co-MOF-MPC-*1* and *3* are shown in Figure S5. Thus, Cu-MOF-MPC-*2*-GCE was selected as an amperometric sensor for hydrazine. Figure 5B exhibits a typical amperometric current-time curve of Co-MOF-MPC-*2*-GCE with successive additions of hydrazine. The best potential to be applied was chosen at +0.2 V based on the CVs measurements. Inset of Figure 5B displays the amperometric response of low concentration of hydrazine at Co-MOF-MPC-*2*-GCE. The relationship between hydrazine concentration and current signal for Co-MOF-MPC-*2*-GCE is illustrated in Figure 5C. The hydrazine sensor displays a linear range of 5 and 630 μM (R^2 =0.998, n=24) with a sensitivity of 216 $\mu A \mu M^{-1}$ and0.63 to 5.40 mM (R^2 = 0.999, n = 13) with a sensitivity of 132.4 $\mu A \mu M^{-1}$. Therefore, the detection limit is calculated as 1.75 μM (S/N=3). To evaluate the

selectivity of the Co-MOF-MPC-*2*-GCE in the detection of hydrazine, we investigated the influence of several ions that could serve as potential interferences in the electrochemical experiments (Fig. S6). For 0.5 mM hydrazine, an ignorable interference was observed for the following ions: Na^+, K^+, Ac^-, NO_3^-, CO_3^{2-}, SO_4^{2-}, and PO_4^{3-} with their concentrations of 100-fold higher than that of hydrazine. The results show good ability of anti-interference of the Co-MOF-MPC-*2*-GCE. The reproducibility of the sensor was also investigated by current-time method for five repetitive measurements with additions of hydrazine concentration of 0.5 mM. The relative standard deviation (RSD) of the current signal for 0.5 mM hydrazine was less than 3%. When the Co-MOF-MPC-*2*-GCE was stored at 4 ℃ for two weeks, the current response to 0.5 mM hydrazine remained 93.2% of its original value, suggesting the long-term stability of the electrode. The performance of the Co-MOF-MPC-*2*-GCE was also compared with that of other hydrazine sensors (Table S3).

The electrocatalytic properties of the different electrodes toward nitrobenzene detection were also investigated. Figure 6A displays the CVs behaviors of the bare GCE, Co-MOF-GCE, MPC-GCE and Co-MOF-MPC-*2*-GCE for nitrobenzene over a potential range between 0.2 and -1.0 V at a scan rate of 50 mV s^{-1}. Clearly, there is a small electrochemical response at bare GCE. However, it shows a significantly enhanced electrochemical response towards nitrobenzene reduction after the modification by the Co-MOF or MPC. Additionally, the Co-MOF-MPC-*2* sample performs the best electrocatalytic activity towards nitrobenzene reduction among the

synthesized electrode materials. The reduction of nitrobenzene for Co- MOF-MPC-*1* and *3* are shown in Figure S7. Thus, we focused on the investigation of the nitrobenzene at the Co-MOF-MPC-*2*-GCE. In this study, the differential pulse voltammetry (DPV) was employed to detect nitrobenzene at Co-MOF-MPC-*2*-GCE (Figure 6B). Obviously, a series of the DPV curves was obtained from different concentrations of nitrobenzene. The calibration curve of reduction current is depicted in Figure 6C, which exhibits steady DPV curves toward nitrobenzene in the linear concentration range of 0.5-15 μM with a sensitivity of 1780 $\mu A \mu M^{-1}$ and 15 to 235 μM with a sensitivity of 1060 $\mu A \mu M^{-1}$. The detection limit is 0.21 μM (S/N=3). The reproducibility of the sensor was also investigated by DPV method. Possible interferences for the detection of nitrobenzene at the Co-MOF-MPC-*2*-GCE were also investigated by addition of various ions and organic pollutants in the presence of 100 μM nitrobenzene (Fig. S8). From the results, Na^+, K^+, CO_3^{2-}, SO_4^{2-}, PO_4^{3-}, NO_3^-, Ac^-, and hydrazine have no obvious influence on the nitrobenzene detection at Co-MOF-MPC-*2*-GCE with their concentrations of 100-fold higher than that of nitrobenzene. The interference of organic compounds, namely aniline, 2-toluidine, toluene, and phenol were tested under the optimized experimental conditions. It was also found that these organic compounds have no response when their concentrations were 10-fold higher than nitrobenzene in this potential range. These imply that the Co-MOF-MPC-*2*-GCE has excellent anti-interference ability. The RSD of current signal for 100 μM nitrobenzene was less than 3.2% for five measurements for the same electrode. After being stored at 4 °C for two weeks, 9.3% current loss at

Co-MOF-MPC-*2*-GCE was obtained by the amperometric response of 100 μM nitrobenzene. The detailed comparison of nitrobenzene detection performance using different nitrobenzene sensors is summarized in Table S4.

4. Conclusions

This work reports on the preparation of a novel Co-MOF-MPC composite by an easy one-step hydrothermal synthesis method. The Co-MOF-MPC-*x* samples have been synthesized with different MPC contents. These materials were verified by detailed characterization analyses and electrochemical investigation. It is found that the nanosized and nanocrystalline Co-MOF obtained by the incorporation of MPC greatly improved the electrochemical activity of the composite. This composite displays excellent electrocatalytic ability for the oxidation of hydrazine and reduction of nitrobenzene compared to the individual counterparts. A sensitive electrochemical sensor for hydrazine and nitrobenzene was developed based on the Co-MOF-MPC-*2*, which showed wide linear range, low detection limit, high sensitivity, and good stability. As a result, successful fabrication of Co-MOF-MPC not only promotes the development of new porous composite materials, but also holds great promise for the design of electrochemical sensors.

Acknowledgements

The authors gratefully acknowledge the financial support of the National Natural Science Foundation of China (21075014), the Fundamental Research Funds for the Central Universities (No.14ZZ2225 and 14QNJJ011) and China Postdoctoral Science Foundation funded project (2014M550164).

References

1. O. K. Farha, A. Özgür Yazaydın, I. Eryazici, C. D. Malliakas, B. G. Hauser, M. G. Kanatzidis, S. T. Nguyen, R. Q. Snurr and J. T. Hupp, *Nat. Chem*., 2010, **2**, 944-948.
2. S. S. Kaye, A. Dailly, O. M. Yaghi and J. R. Long, *J. Am. Chem. Soc*., 2007, **129**, 14176-14177.
3. J.-R. Li, R. J. Kuppler and H.-C. Zhou, *Chem. Soc. Rev*., 2009, **38**, 1477-1504.
4. J. An, S. J. Geib and N. L. Rosi, *J. Am. Chem. Soc*., 2009, **131**, 8376-8377.
5. P. Horcajada, C. Serre, M. Vallet-Regí, M. Sebban, F. Taulelle and G. Férey, *Angew. Chem. Int. Ed*., 2006, **45**, 5974-5978.
6. A. Dhakshinamoorthy, M. Alvaro and H. Garcia, *Chem. Commun*., 2012, **48**, 11275-11288.
7. Z.-Z. Lu, R. Zhang, Y.-Z. Li, Z.-J. Guo and H.-G. Zheng, *J. Am. Chem. Soc*., 2011, **133**, 4172-4174.
8. D. Ma, B. Li, X. Zhou, Q. Zhou, K. Liu, G. Zeng, G. Li, Z. Shi and S. Feng, *Chem. Commun*., 2013, **49**, 8964-8966.
9. C.-X. Yang, H.-B. Ren and X.-P. Yan, *Anal. Chem*., 2013, **85**, 7441-7446.
10. J. Xiao, Y. Wu, M. Li, B. Y. Liu, X. C. Huang and D. Li, *Chem. Eur. J*., 2013, **19**, 1891-1895.
11. J. Mao, L. Yang, P. Yu, X. Wei and L. Mao, *Electrochem. Commun*., 2012, **19**, 29-31.

12. R. Senthil Kumar, S. Senthil Kumar and M. Anbu Kulandainathan, *Electrochem. Commun*., 2012, **25**, 70-73.

13. P. Pachfule, B. K. Balan, S. Kurungot and R. Banerjee, *Chem. Commun*., 2012, **48**, 2009-2011.

14. D. Qian, C. Lei, G.-P. Hao, W.-C. Li and A.-H. Lu, *ACS Appl. Mater. Interfaces*, 2012, **4**, 6125-6132.

15. Z. Xiang, Z. Hu, D. Cao, W. Yang, J. Lu, B. Han and W. Wang, *Angew. Chem. Int. Ed*., 2011, **50**, 491-494.

16. C. Petit and T. J. Bandosz, *Adv. Mater*., 2009, **21**, 4753-4757.

17. J. H. Lee, S. Kang, J. Jaworski, K.-Y. Kwon, M. L. Seo, J. Y. Lee and J. H. Jung, *Chem. Eur. J*., 2012, **18**, 765-769.

18. M. Jahan, Q. Bao, J.-X. Yang and K. P. Loh, *J. Am. Chem. Soc*., 2010, **132**, 14487-14495.

19. M. Jahan, Q. Bao and K. P. Loh, *J. Am. Chem. Soc*., 2012, **134**, 6707-6713.

20. M. Jahan, Z. Liu and K. P. Loh, *Adv. Funct.Mater*., 2013, **23**, 5363-5372.

21. Y. Zhang, X. Bo, C. Luhana, H. Wang, M. Li and L. Guo, *Chem. Commun*., 2013, **49**, 6885-6887.

22. Y. Zhang, L. Zeng, X. Bo, H. Wang and L. Guo, *Anal. Chim. Acta*, 2012, **752**, 45-52.

23. Y. Zhang, X. Bo, A. Nsabimana, H. Wang, M. Li and L. Guo, *Analyst*, 2013, **138**, 3633-3637.

24. F. Yang, B. Li, W. Xu, G. Li, Q. Zhou, J. Hua, Z. Shi and S. Feng, *Inorg. Chem*., 2012, **51**, 6813-6820.

25. S. Jun, J. S. Hoon, R. Ryoo, M. Kruk, M. Jaroniec, Z. Liu, T. Ohsuna and O. Terasaki, *J. Am. Chem. Soc.* 2000, **122**, 10712-10713.

26. W. Stöber, A. Fink and E. Bohn, *J. Colloid Interface Sci.* 1968, **26**, 62-69.

27. S. S. Tandon, L. K. Thompson, M. E. Manuel and J. N. Bridson, *Inorg. Chem*., 1994, **33**, 5555-5570.

Figure captions

Scheme 1 Illustration of the preparation of Co-MOF-MPC.

Figure 1 (A): XRD patterns of MPC (a), pure Co-MOF (b), and Co-MOF-MPC-*1*, *2*, and *3* (c, d, and e). (B): FT-IR spectroscopy of pure Co-MOF (a) and Co-MOF-MPC-*1*, *2*, and *3* (b, c, and d). TGA (C) and DTG (D) curves of pure Co-MOF (a) and Co-MOF-MPC-*2* (b) at air atmosphere.

Figure 2 SEM images of MPC (A), pure Co-MOF (B), and Co-MOF-MPC-*2* (C). EDX spectra of Co-MOF-MPC-*2* (D).

Figure 3 XPS spectra in the region of Co $2p_{3/2}$ and Co $2p_{1/2}$ peaks of pure Co-MOF (A) as well as Co-MOF-MPC-*1*, *2*, and *3* (B, C, and D).

Figure 4 EIS of as-prepared products in a 0.1 M KCl solution containing 5.0 mM $K_3Fe(CN)_6/K_4Fe(CN)_6$ and from 0.1 Hz to 10.0 KHz. Inset: the EIS curve of pure Co-MOF.

Figure 5 (A): CVs of as-prepared products modified GCE in the absence (black line) and presence (red line) of 0.5 mM hydrazine. (B): Typical amperometric current-time curve of Co-MOF-MPC-*2*-GCE with successive additions of hydrazine. (C): Relationship between hydrazine concentration and current signal for Co-MOF-MPC-*2*-GCE.

Figure 6 (A): CVs of as-prepared products modified GCE in the absence (black line) and presence (red line) of 100 μM nitrobenzene. (B): DPV curves of nitrobenzene:

0.5, 2.5, 5, 7.5, 10, 12.5, 15, 35, 55, 75, 95, 115, 175, and 235 μM in 0.1M NaOH at Co-MOF-MPC-*2*-GCE. (C): Relationship between nitrobenzene concentration and current signal for Co-MOF-MPC-*2*-GCE.

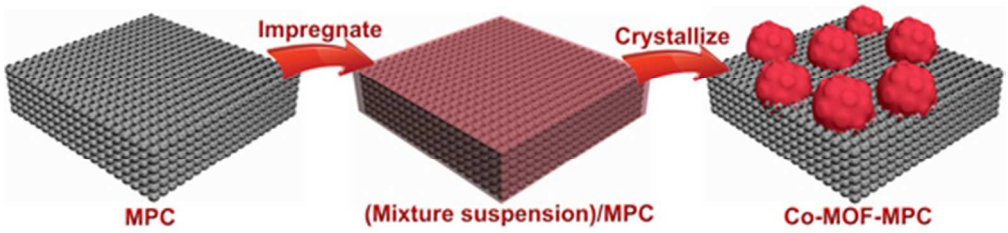

Illustration of the preparation of Co-MOF-MPC.
45x11mm (300 x 300 DPI)

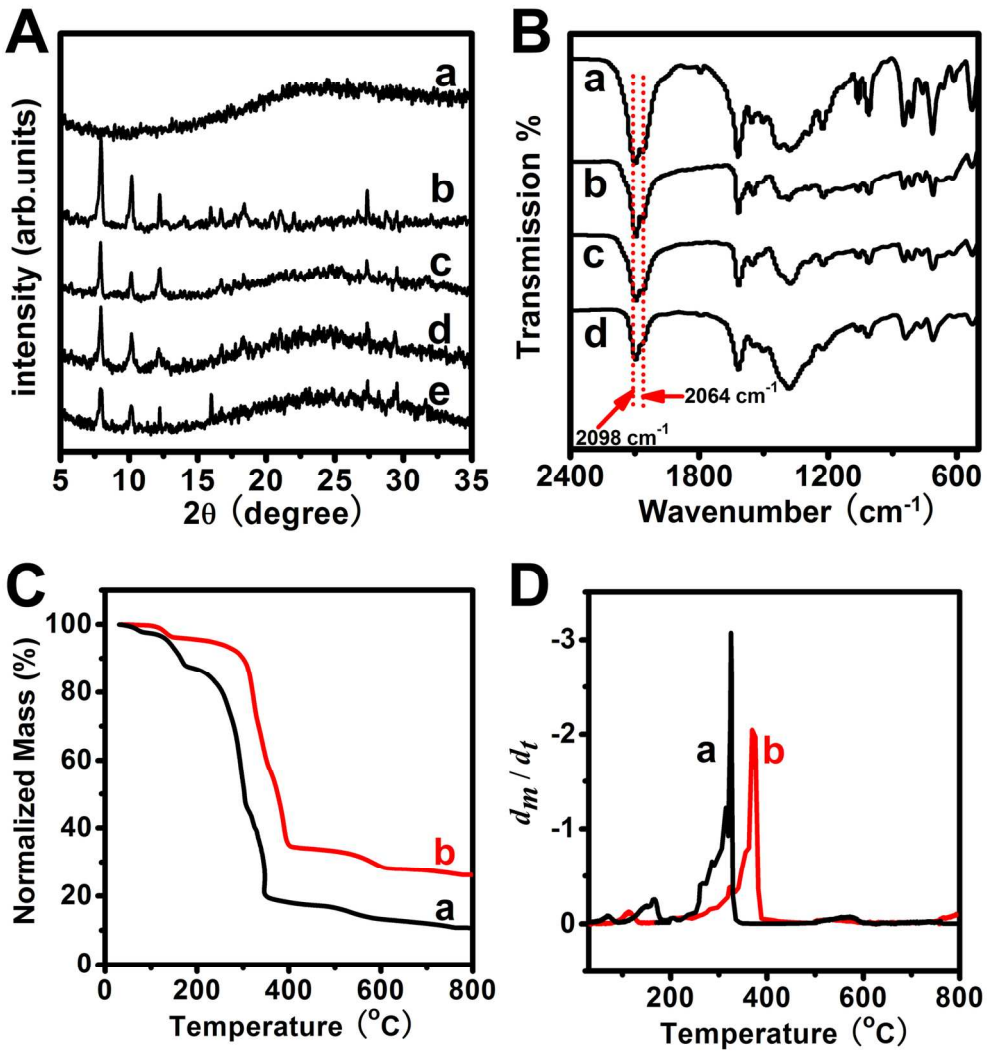

(A): XRD patterns of MPC (a), pure Co-MOF (b), and Co-MOF-MPC-1, 2, and 3 (c, d, and e). (B): FT-IR spectroscopy of pure Co-MOF (a) and Co-MOF-MPC-1, 2, and 3 (b, c, and d). TGA (C) and DTG (D) curves of pure Co-MOF (a) and Co-MOF-MPC-2 (b) at air atmosphere.
151x163mm (300 x 300 DPI)

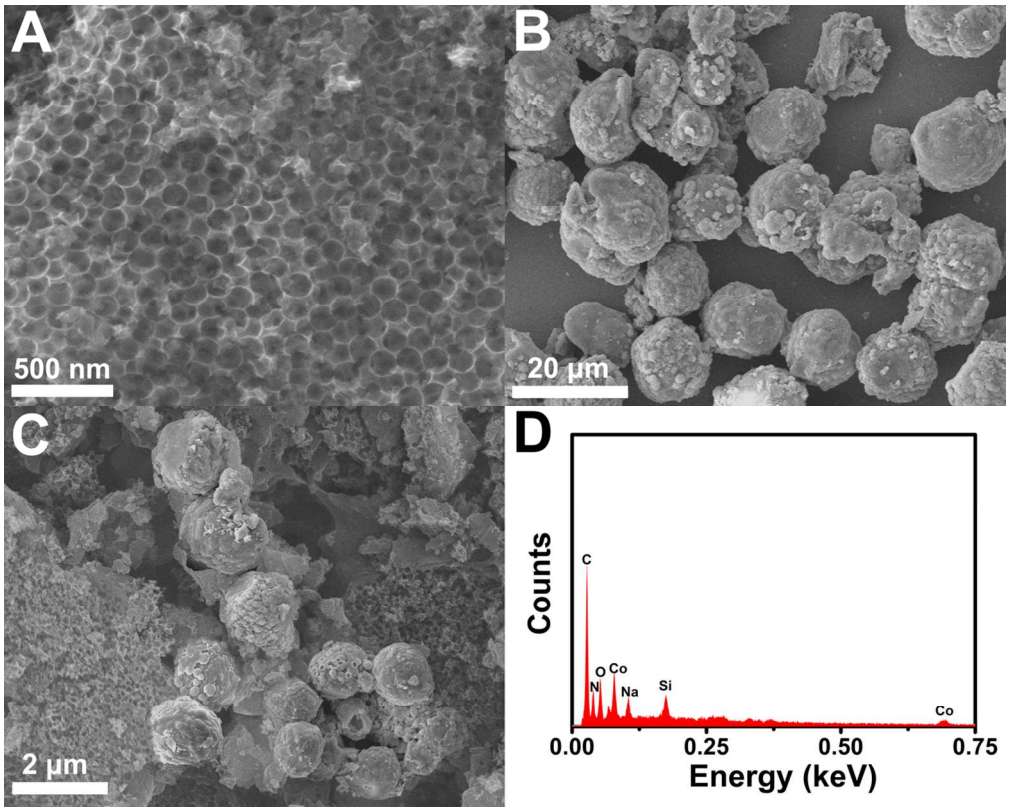

SEM images of MPC (A), pure Co-MOF (B), and Co-MOF-MPC-2 (C). EDX spectra of Co-MOF-MPC-2 (D).
119x96mm (300 x 300 DPI)

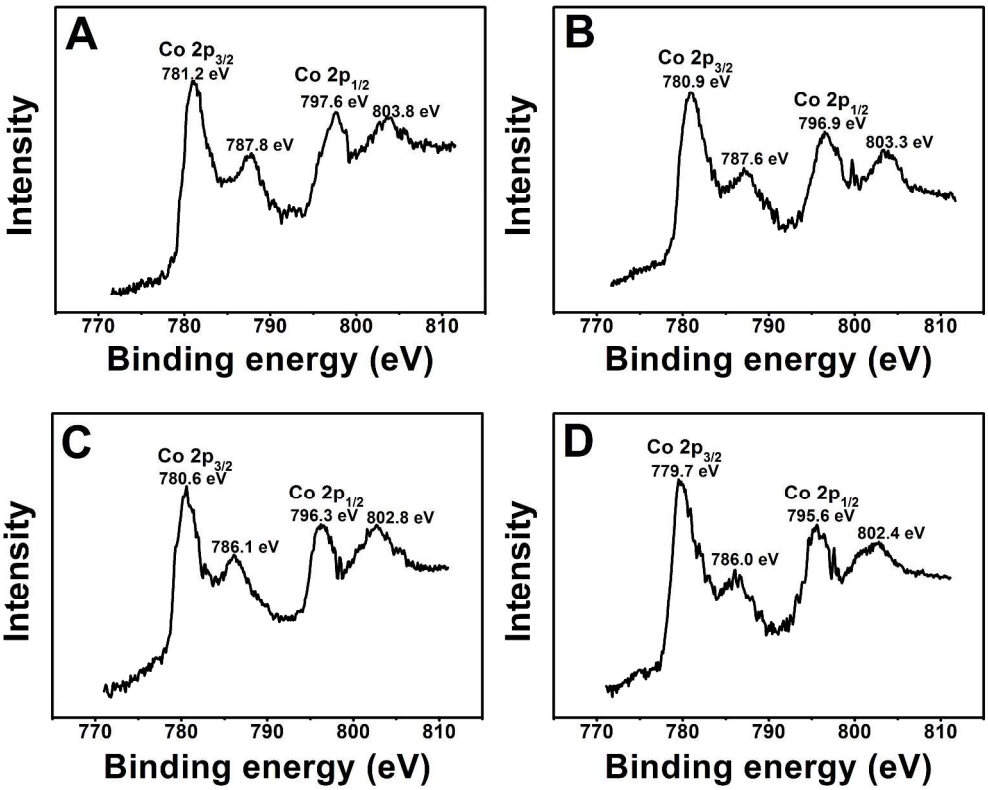

XPS spectra in the region of Co 2p3/2 and Co 2p1/2 peaks of pure Co-MOF (A) as well as Co-MOF-MPC-1, 2, and 3 (B, C, and D).
449x364mm (300 x 300 DPI)

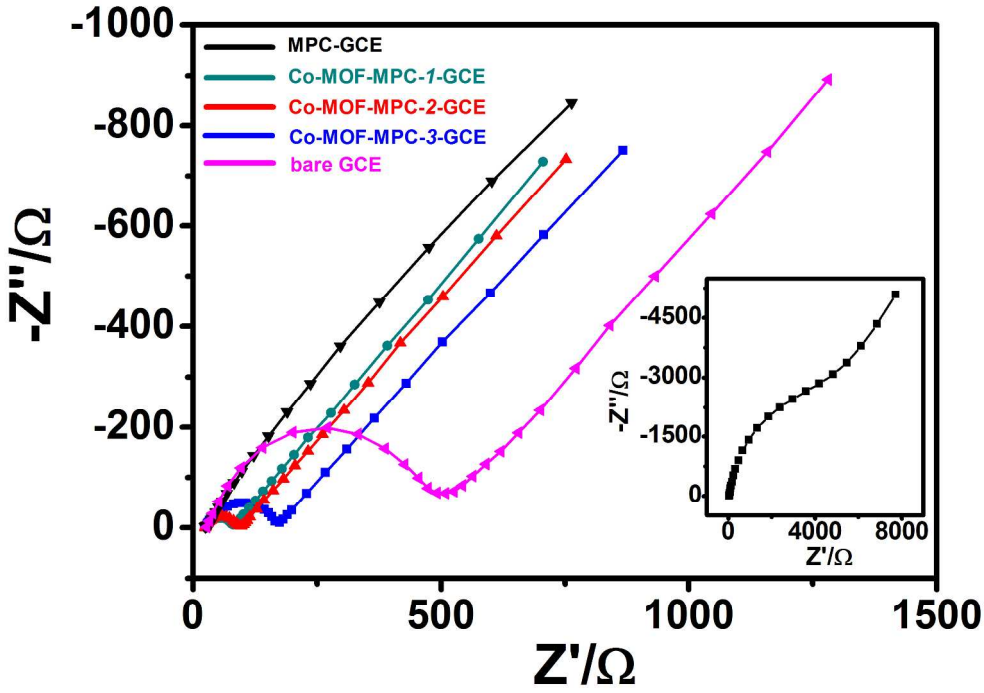

EIS of as-prepared products in a 0.1 M KCl solution containing 5.0 mM K3Fe(CN)6/K2Fe(CN)6 and from 0.1 Hz to 10.0 KHz. Inset: the EIS curve of pure Co-MOF.
272x195mm (300 x 300 DPI)

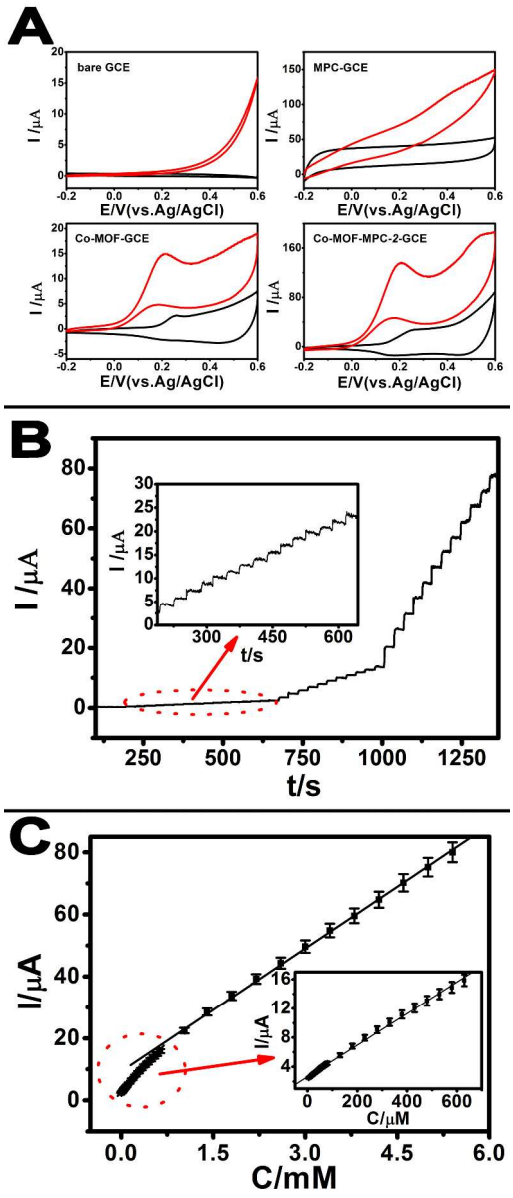

(A): CVs of as-prepared products modified GCE in the absence (black line) and presence (red line) of 0.5 mM hydrazine. (B): Typical amperometric current-time curve of Co-MOF-MPC-2-GCE with successive additions of hydrazine. (C): Relationship between hydrazine concentration and current signal for Co-MOF-MPC-2-GCE.
237x564mm (300 x 300 DPI)

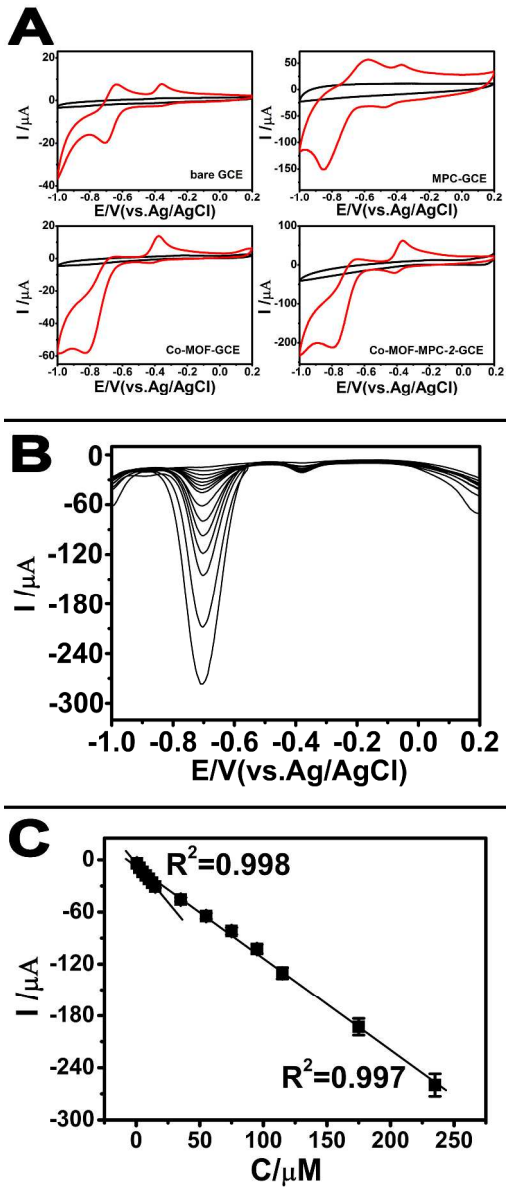

(A): CVs of as-prepared products modified GCE in the absence (black line) and presence (red line) of 100 μM nitrobenzene. (B): DPV curves of nitrobenzene: 0.5, 2.5, 5, 7.5, 10, 12.5, 15, 35, 55, 75, 95, 115, 175, and 235 μM in 0.1M NaOH at Co-MOF-MPC-2-GCE. (C): Relationship between nitrobenzene concentration and current signal for Co-MOF-MPC-2-GCE.
237x569mm (300 x 300 DPI)

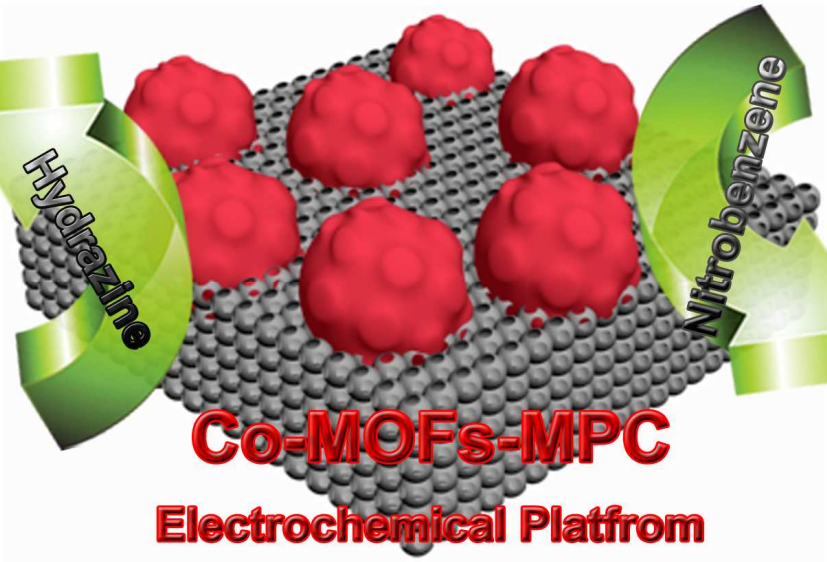

Preparation of novel cobalt-based MOFs with incorporated macroporous carbon composite for enhanced electrocatalytic ability for hydrazine and nitrobenzene.